

1 Supporting information

2 **Brownian dynamics simulation of the diffusion of rod-like nanoparticle in** 3 **polymeric gels**

4 Mohammad-Reza Rokhforouz¹, Don D Sin², Sarah Hedtrich³⁻⁵, and James J Feng^{1,6*}

5 ¹Department of Chemical and Biological Engineering, University of British Columbia, Vancouver, British
6 Columbia, Canada

7 ²Centre for Heart Lung Innovation, University of British Columbia, Vancouver, British Columbia, Canada

8 ³Faculty of Pharmaceutical Sciences, University of British Columbia, Vancouver, British Columbia, Canada

9 ⁴School of Biomedical Engineering, University of British Columbia, Vancouver, British Columbia, Canada

10 ⁵Center of Biological Design, Berlin Institute of Health at Charité – Universitätsmedizin Berlin, Germany

11 ⁶Department of Mathematics, University of British Columbia, Vancouver, British Columbia, Canada

12 *Corresponding author: james.feng@ubc.ca

13 **S1. Nanorod and gel properties**

14 In the hd-protocol of varying the length and diameter of the rod-like nanoparticle (RNP), the
15 hydrodynamic diameter d_H is kept constant (Eq. 1 of the main text). Most of the simulations are
16 based on $d_H = 160$ nm. The dimensions of the RNP at different aspect ratios is given in Table S1
17 below.

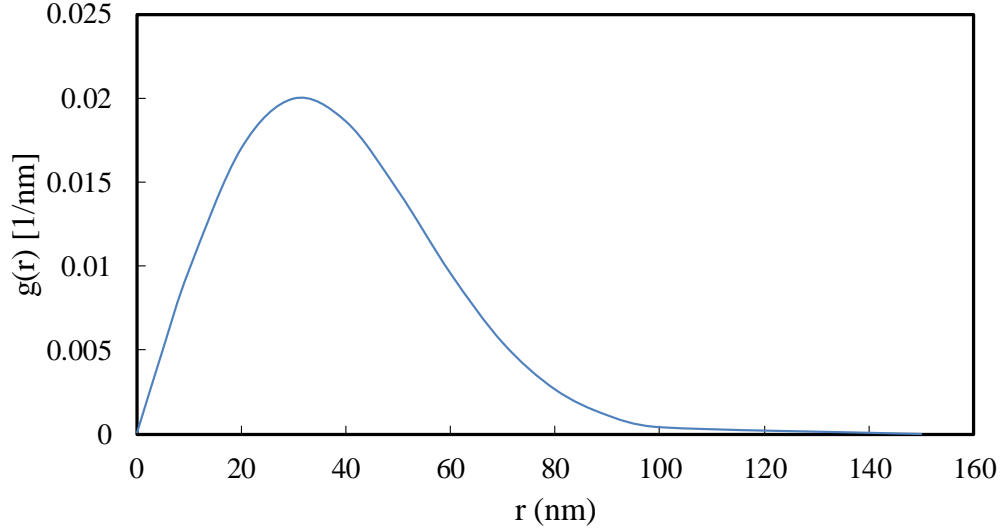
18 Table S1. Nanorod dimensions for different aspect ratio values when $d_H = 160$ nm

Aspect ratio (λ)	Diameter (nm)	Length (nm)
1	138.52	138.52
2	104.80	209.60
3	85.95	257.87
4	73.62	294.51
5	64.83	324.17

19 For a random network of straight thin fibers, Ogston¹ formulated the pore size distribution in terms
20 of the radii of the largest spheres that can fit into the pores:

$$g(r) = (4\pi\nu L_f r + 4\pi\nu r^2) \exp\left[-\left(2\pi\nu L_f r^2 + \frac{4\pi}{3}\nu r^3\right)\right] \quad (\text{S1})$$

21 where $g(r)$ is the distribution function, r is the pore radius, ν is the number of fibers per unit volume,
22 and L_f is the half-length of the fibers. Fig. S1 shows the variation of $g(r)$ as a function of r when
23 $2\nu L_f = 16 \times 10^{13} \text{ m}^{-2}$ and $2L_f = 1 \mu\text{m}$ (See Table 1).



24

25

Fig. S1 Variation of $g(r)$ as a function of r for the gel specified in Table 1.

26

S2. Discretized governing equations:

27

28

29

Following Löwen,² we develop the finite-difference schemes for temporal discretization of our governing equations, Eqs. (2–4) in the main text. To advance the parallel component of \mathbf{R} in time, Eq. (2) is discretized as

$$\mathbf{R}^{\parallel}(t + \Delta t) = \mathbf{R}^{\parallel}(t) + \frac{1}{\zeta^{\parallel}} \mathbf{F}_{ext}^{\parallel}(t) \Delta t + \Delta R^{\parallel} \boldsymbol{\Omega}(t), \quad (\text{S2})$$

30

31

where Δt is the time step, and ΔR^{\parallel} is a random displacement due to collisions with solvent molecules. It is a Gaussian-distributed random number with zero mean, and variance

$$\overline{(\Delta R^{\parallel})^2} = 2D_0^{\parallel} \Delta t. \quad (\text{S3})$$

32

Here, $\overline{(\)}$ denotes an average over a Gaussian distribution.

33

34

The perpendicular component, on the other hand, diffuses with the perpendicular diffusion constant D_0^{\perp} :

$$\mathbf{R}^{\perp}(t + \Delta t) = \mathbf{R}^{\perp}(t) + \frac{1}{\zeta^{\perp}} \mathbf{F}_{ext}^{\perp}(t) \Delta t + \Delta R_1^{\perp} \mathbf{e}_1(t) + \Delta R_2^{\perp} \mathbf{e}_2(t), \quad (\text{S4})$$

35 where again $\Delta\mathbf{R}_1^\perp$ and $\Delta\mathbf{R}_2^\perp$ are Gaussian random displacements with zero mean and variance
 36 $2D_0^\perp\Delta t$. After \mathbf{R}^\perp and \mathbf{R}^\parallel are evaluated at the new time, the particle position is updated as
 37 $\mathbf{R} = \mathbf{R}^\parallel + \mathbf{R}^\perp$.

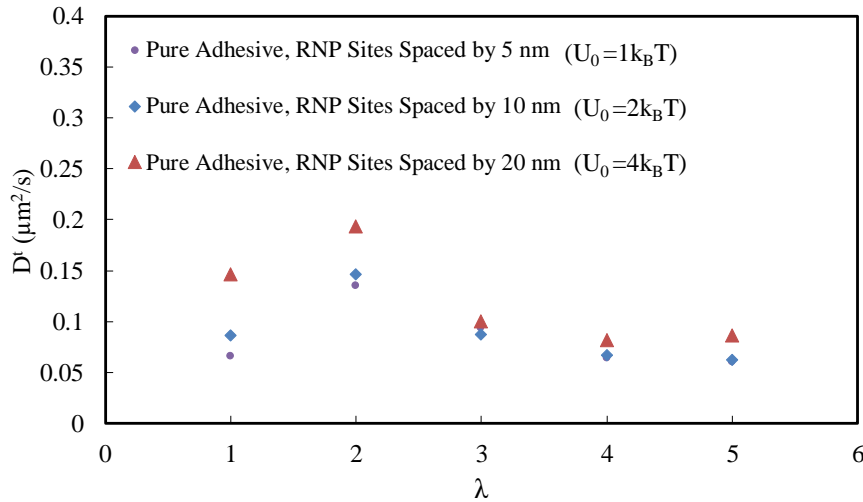
38 Finally, the orientation of the RNP long axis diffuses as

$$\mathbf{\Omega}(t + \Delta t) = \mathbf{\Omega}(t) + \frac{1}{\zeta^r} \mathbf{T}_{ext}(t) \times \mathbf{\Omega}(t) \Delta t + x_1 \mathbf{e}_1(t) + x_2 \mathbf{e}_2(t), \quad (\text{S5})$$

39 where $\mathbf{T}_{ext}(t)$ is the external torque acting on the rod and x_1, x_2 are Gaussian random numbers
 40 with zero mean and variance $2D_0^r\Delta t$. After each step, the orientation vector is rescaled to have
 41 unit norm.

42 **S3. Discretization of rod-like nanoparticles in adhesive interaction**

43 To ensure that our results are not influenced by the discretization of the RNP, we examine three
 44 cases: discretizing the RNP length into segments of 5 nm, 10 nm (our baseline case), and 20 nm.
 45 To maintain a fair comparison, we keep the total adhesion potential constant, meaning that in cases
 46 with a sparser distribution (e.g., 20 nm), individual adhesion sites will have a higher U_0 . Fig. S2
 47 illustrates the variation in translational diffusivity as a function of aspect ratio. As shown, all cases
 48 exhibit a similar non-monotonic trend, confirming that the discretization of adhesion sites does not
 49 significantly affect the results. The difference between the 3 cases is more noticeable for rods with
 50 smaller λ . This is because we have fewer integration points on these short and thick RNPs, e.g.,
 51 only 7 points for $\lambda = 1$ at $U_0 = 4k_B T$.



52
 53 Fig. S2 Effect of RNP discretization on the translational diffusivity D^t with purely adhesive
 54 interaction. The nominal separation between neighboring adhesion sites on the fibers is $r_0 =$
 55 200 nm. The RNP hydrodynamic diameter is $d_H = 160$ nm.

56 **S4. Statistical analysis:**

57 Our BD simulation tracks the trajectory of P particles, each governed by the Langevin equations
 58 (Eqs. 2–4) and starting from a randomly chosen location and orientation. For each of the P
 59 individual trajectories, we use internal sampling³ over all pairs of points as a function of the time
 60 interval t :

$$61 \quad \overline{R^2(t)} = \frac{1}{Q} \sum_{k=1}^M |R(t_k + t) - R(t_k)|^2 \quad (S6)$$

62 where Q is the number of all pairs separated by t , $t_k = (k-1)\Delta t$ is the starting time of the k^{th} time
 63 step and the starting time of the k^{th} pair, and $\overline{R^2(t)}$ is the single-particle mean squared
 64 displacement (MSD). Moreover, we ensemble-average over all the P non-interacting trajectories:

$$65 \quad \langle \overline{R^2(t)} \rangle = \frac{1}{P} \sum_{i=1}^P \overline{R_i^2(t)} \quad (S7)$$

66 to compute the ensemble MSD $\langle \overline{R^2(t)} \rangle$ (we will simply call it MSD). Finally, the long-time
 67 translational diffusion coefficient, D_L^t , is calculated as:⁴

$$68 \quad D_L^t = \lim_{t \rightarrow \infty} \frac{\langle \overline{R^2(t)} \rangle}{6t} \quad (S8)$$

69 The long-time limit is reached when the ensemble-averaged MSD varies linearly with time. We
 70 have compared the above method with an ensemble averaging without internal sampling and found
 71 that the internal sampling effectively reduced the statistical noise by extracting more information
 72 from each particle trajectory.⁵ In addition, we have validated our numerical scheme against
 73 analytical formulas of the diffusivity for free-diffusion⁶ and numerical simulations of rod-rod
 74 interaction.⁷

75 The long-time orientational self-diffusion coefficient D_L^r , on the other hand, is defined via the
 76 long-time limit of a diffusive process on the unit sphere:²

$$D_L^r = \lim_{t \rightarrow \infty} D^r(t) \quad (S9)$$

77 with

$$D^r(t) = -\frac{1}{2t} \ln [\langle \mathbf{\Omega}(0) \cdot \mathbf{\Omega}(t) \rangle]. \quad (S10)$$

78 **S5. Distinguishing the meandering and directional modes**

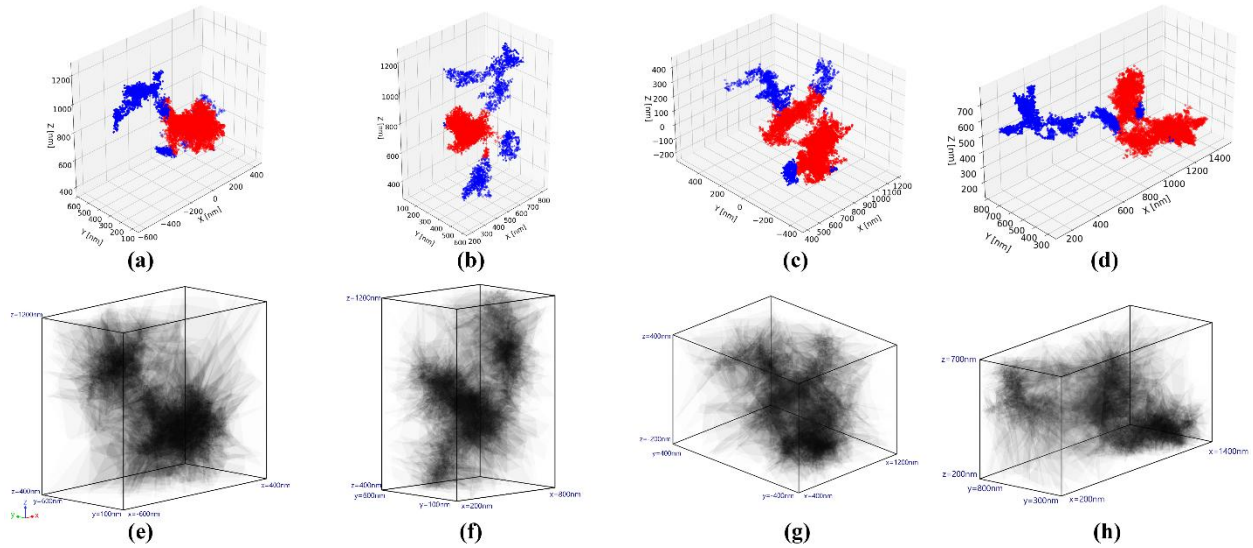
79 To quantitatively distinguish the meandering and directional modes of diffusion, and to determine
80 their respective prevalence, we have used two different methods to characterize the points on the
81 trajectories of the RNP centroid.

82 (a) Cluster analysis based on the Density-Based Spatial Clustering of Applications with Noise
83 (DBSCAN) algorithm.⁸ DBSCAN divides the trajectory into “clusters” of closely positioned
84 points, and “noise” consisting of points not belonging to any cluster. In this algorithm, data points
85 are classified into three categories: (i) core points, which are surrounded by a minimum number of
86 neighboring points (minPts) within a specified radius (eps), (ii) border points, which are adjacent
87 to core points but do not have enough neighbors to be core points themselves, and (iii) noise points,
88 which do not belong to any cluster. We interpret the clusters formed by core and border points as
89 meandering episodes, while the noise points correspond to directional episodes. For this analysis,
90 we set $\text{eps} = 100 \text{ nm}$ and $\text{minPts} = 1000$.

91 (b) Voronoi tessellation. For the set of points on a trajectory, e.g., those of Fig. 5(b), we divide the
92 spatial domain into interlocking cells “centered” on each trajectory point. More precisely, each
93 Voronoi cell contains all the spatial points that are closer to its trajectory point than to any other
94 trajectory points. Voronoi analysis is particularly useful for quantifying the available space around
95 each point, as the size and shape of each cell reflect the local density and arrangement of the
96 points.⁹ Unlike the DBSCAN method, which requires two user-defined parameters, Voronoi
97 tessellation requires no manual input and yields a unique, parameter-free result. Although
98 originally introduced to study crystalline structures, Voronoi analysis has been widely applied to
99 characterize the local geometry in soft matter systems as well. Here, we employed the OVITO
100 software package to compute the Voronoi tessellation.¹⁰

101 Fig. S3 illustrates four representative trajectories analyzed with DBSCAN and Voronoi
102 tessellation. The clusters identified by DBSCAN (top panel), shown in red, correspond to the
103 meandering phase. In contrast, the noise points, displayed in blue and generally appearing as
104 thinner, narrower branches, represent the directional mode. The Voronoi analysis (bottom panel)
105 produces darker regions with denser and smaller cells that correspond to the meandering mode,
106 and lighter regions with more sparse and larger cells that correspond to the directional mode. Thus,
107 the two modes of diffusion can be identified and distinguished using either methods. Fig. S3 shows
108 that the two yield consistent outcomes. In DBSCAN, the distinction between clusters and outliers
109 is made somewhat arbitrarily by the parameters eps and minPts . In Voronoi analysis, similarly,
110 one would need to specify a threshold cell volume or density to demarcate the two modes of
111 diffusion. The exact boundary between the modes is subject to such parameter choices.

112 Once we identify the meandering and directional episodes using either method, we can measure
113 the residence time of the RNP in each mode. Results generally show that the meandering mode
114 has a much longer residence time. Counting the duration of the multiple episodes in multiple
115 trajectories, we find that on average, the meandering mode is about three times as prevalent as the
116 directional mode, occupying roughly 75% of the time. This supports the argument that the
117 diffusing RNP experiences a skewed pore-size distribution much in favor of the larger pores.



118

119 Fig. S3 Four representative trajectories for analyzing the two modes of diffusion. (a-d) Clusters
 120 (red) and noise points (blue) identified by DBSCAN. (e-h) The Voronoi cells around the trajectory
 121 points. Darker areas correspond to small cell volume and higher cell density.

122

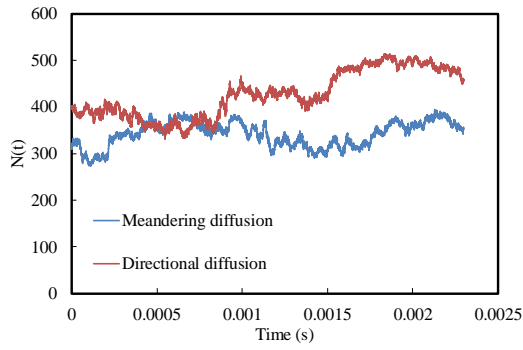
123 **S6. Parametric study of the crowdedness number $N(t)$**

124 In the main text, the crowdedness number $N(t)$ is computed from Eq. (17). To verify that the
 125 observed trend in $N(t)$ does not depend on the parameters n_f (number of discrete segments on each
 126 fiber of the gel network), n_r (number of discrete segments on the RNP), and l_e (cutoff distance for
 127 counting neighboring segments), we conduct numerical experiments by varying these parameters
 128 one at a time. Fig. S4 illustrates the variation of $N(t)$ for different parameter sets. As expected, the
 129 pairwise neighbor counts N is higher for larger n_f (Fig. S4(a) and (b)) and larger l_e (Fig. S4(e) and
 130 (f)). With increasing n_r , the increase in neighbor counts is minimal (Fig. S4(c) and (d)). This is
 131 because in the definition of N in Eq. (17), one counts each fiber segment only once. For newly
 132 inserted RNP segments, there would be few fiber segments available to form new pairs and to add
 133 to N . Thus, N saturates quickly with increasing n_r .

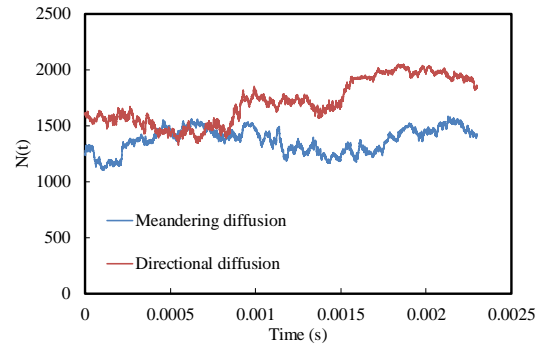
134 All these cases bear out the same trend as shown by Fig. 6(c) of the main text: the surrounding
 135 fiber network is denser and more crowded during the directional diffusion than the meandering
 136 diffusion.

137

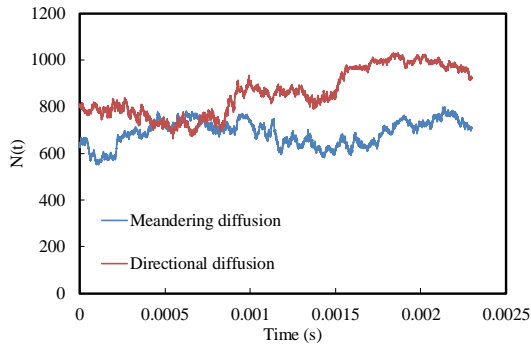
138



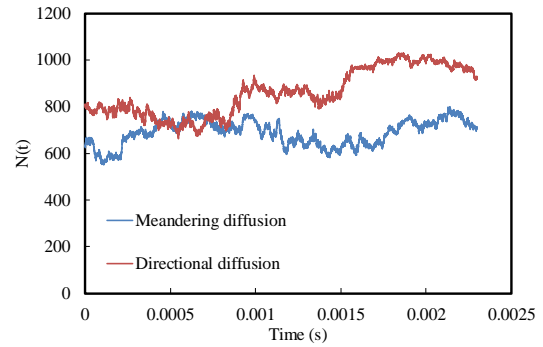
(a)



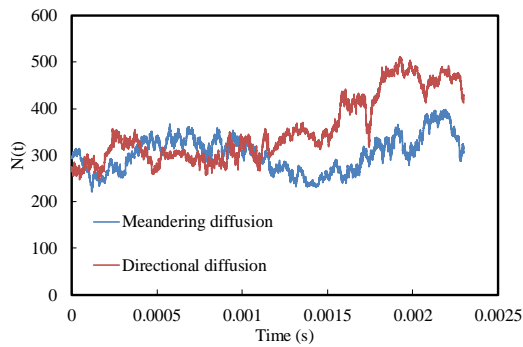
(b)



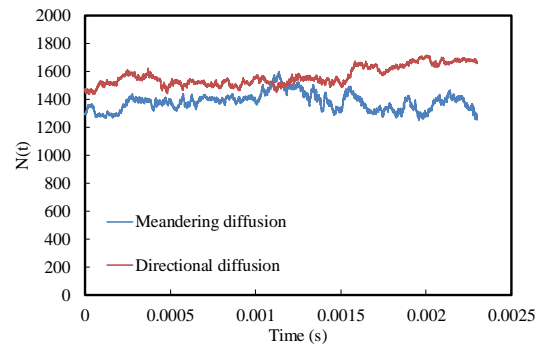
(c)



(d)



(e)



(f)

139 Fig. S4 Parametric studies of $N(t)$. The base parameters are $n_r = 3$, $n_f = 100$, and $l_e = 200$ nm. Each
 140 subfigure shows the effect of varying one parameter: (a) $n_f = 50$, (b) $n_f = 200$, (c) $n_r = 6$, (d) $n_r = 9$,
 141 (e) $l_e = 150$ nm, and (f) $l_e = 250$ nm.

142

143 **References:**

- 144 1 A. G. Ogston, *Trans. Faraday Soc.*, 1958, **54**, 1754–1757.
- 145 2 H. Löwen, *Phys. Rev. E*, 1994, **50**, 1232.
- 146 3 M. J. Saxton, *Biophys. J.*, 1997, **72**, 1744–1753.
- 147 4 J. Hansing, C. Ciemer, W. K. Kim, X. Zhang, J. E. DeRouchey and R. R. Netz, *Eur. Phys. J. E*,
148 2016, **39**, 1–13.
- 149 5 B. Tafech, M. R. Rokhforouz, J. Leung, M. M. H. Sung, P. J. C. Lin, D. D. Sin, D. Lauster, S.
150 Block, B. S. Quon, Y. Tam, P. Cullis, J. J. Feng and S. Hedtrich, *Adv. Healthc. Mater.*, 2024, **13**,
151 2304525.
- 152 6 M. M. Tirado, C. L. Martínez and J. G. De La Torre, *J. Chem. Phys.*, 1984, **81**, 2047–2052.
- 153 7 J.-Y. Chen, Z. Li, I. Szlufarska and D. J. Klingenberg, *J. Rheol. (N. Y. N. Y.)*, 2021, **65**, 273–288.
- 154 8 M. Ester, H.-P. Kriegel, J. Sander and X. Xu, in *Proceedings of the Second International*
155 *Conference on Knowledge Discovery and Data Mining*, 1996, pp. 226–231.
- 156 9 E. A. Lazar, J. Lu and C. H. Rycroft, *Am. J. Phys.*, 2022, **90**, 469–480.
- 157 10 A. Stukowski, *Model. Simul. Mater. Sci. Eng.*, 2009, **18**, 15012.

158